Tunable Supercontinuum Fiber Laser Source for BRDF Measurements in the STARR II Gonioreflectometer

Heather J. Patrick,[1,*] Clarence J. Zarobila,[1,2] Thomas A. Germer,[1] Victor A. Ying,[1] Catherine A. Cooksey,[1] and Benjamin K. Tsai[1]

[1]National Institute of Standards and Technology, Gaithersburg MD 20899 USA;
[2]Jung Research and Development Corp., Washington DC 20009 USA

ABSTRACT

STARR II is a planned NIST facility for spectral measurements of specular reflectance and diffuse bidirectional reflectance distribution function (BRDF) that is the follow-on to the current NIST STARR (Spectral Tri-function Automated Reference Reflectometer) facility. STARR II will improve and expand on the measurement capabilities of STARR, increasing spectral coverage in the short-wave infrared spectral region and adding out-of-plane BRDF measurement capability. We present characteristics of a tunable light source constructed for STARR II, which is based upon a supercontinuum fiber laser and has a tuning range from 500 nm to 2450 nm, alongside those of the current lamp-based system in STARR. We then discuss considerations for measuring BRDF using this source. The STARR II goniometer will employ an articulated robotic arm to center and orient the sample, and we calculate the transformations from orientation of the sample and receiver to incident and scattering angles for measurements of in-plane and out-of-plane BRDF. We also present, for the first time, an analytic expression for the correction of measured BRDF to true BRDF due to the finite illumination area and collection aperture, and to the effects of uniformity of illumination. Finally, we present exploratory BRDF measurements on a diffuse sample made using the tunable supercontinnum source.

Keywords: supercontinuum, laser, bidirectional, diffuse, BRDF, reflectance, STARR, STARR II

1. INTRODUCTION

Measurements of the diffuse and specular reflectance of materials as a function of wavelength, or spectral reflectance, are used for spectral characterization of mirrors, as input to check reflectance models used in computer rendering and reflectance theory, to develop databases of material reflectance properties, and in the calibration of diffuse reflectance standards. Diffuse reflectance standards are of particular interest in ground- and space-based remote sensing because a calibrated reflectance standard, along with a source of known irradiance such as the sun or standard irradiance lamp, can be used to present a spectral radiance reference for calibration of spectroradiometers. For diffuse scattering surfaces, the reflectance as a function of incidence and viewing angles, wavelength, and polarization is given by the bi-directional reflectance distribution function, or BRDF.

The U.S. national reference instrument for spectral reflectance measurements of spectrally neutral, non-fluorescent samples at room temperature is the NIST Spectral Tri-function Automated Reference Reflectometer (STARR).[1] STARR performs in-plane (meaning the sample normal, illumination axis, and receiver axis are all in a plane) measurements of BRDF. As a calibration service, STARR can measure angle-resolved BRDF from diffuse samples at wavelengths from 250 nm to 1100 nm, with total directional-hemispherical reflectance offered at wavelengths from 250 nm to 2500 nm. While the measurement of angle-resolved BRDF at Short-Wave Infra-Red (SWIR) wavelengths has been demonstrated using STARR, these measurements are challenging due to low source flux at SWIR wavelengths, and are presently limited to the 0:45 reflectance geometry.[2,3] However, there is growing demand to expand NIST's capabilities for BRDF, particularly in the SWIR. For example, remote sensing satellites for climate include spectral bands in the SWIR, and use a diffuse reflectance standard as part of the validation and calibration of their earth-viewing spectroradiometers.[4] Typically, the incident and viewing geometry is not in-plane, but rather out-of-plane, with the view angle azimuthally rotated from the plane of incidence. It is highly desirable to calibrate transfer standards for these systems at the same incident and viewing geometry that will be used in the satellite. Additionally, users in the ground- and ocean-based

---

[*] Corresponding author: heather.patrick@nist.gov

remote sensing community prefer larger reflectance standards than can be accommodated by STARR. These measurement demands are driving the need for a new spectral BRDF facility, STARR II. Among the requirements to be addressed by STARR II are the addition of out-of-plane BRDF measurement capability, with angle-resolved BRDF measurements available in a full hemisphere above the sample surface at all wavelengths, including the SWIR, increased sample size to accommodate samples up to 12 inches on a side, and greatly increased source flux to enable faster measurements with lower uncertainties. The goal is to perform BRDF measurements over a spectral range from 250 nm to 2500 nm, inclusive. To fulfill the need for out-of-plane measurements, STARR II will employ an articulated arm robot inspired by recent work at other national metrology institutes.[5,6] The robot will be used to orient the sample relative to the direction of the incident light, and in combination with a rotating detector arm to collect scattered light, will allow nearly any incident and scattering angle combination to be reached.

We have developed a supercontinuum (SC)-based tunable light source operating from 500 nm to 2450 nm for STARR II, along with beam delivery optics to produce a well-focused, 1 cm diameter illumination spot at the sample plane of the future robot-based goniometer. This light source, along with a prototype receiver to collect scattered light, is being used in a manual mode to perform BRDF measurements at in-plane geometries. In this paper, we demonstrate characteristics of the STARR II light source and compare with the current lamp-based STARR light source. Power versus wavelength and polarization state, and measurements of the beam profile at the sample plane will be presented for both STARR and STARR II. We then consider the corrections to the ideal BRDF measurement equation, applicable to any BRDF measurement instrument with a finite illumination and collection aperture, which arise from the finite size of the illuminated area on the sample, the finite size of the collection aperture, and the non-uniformity of the illumination intensity over the illuminated area. We show that the part of the correction due to finite non-uniform illumination can be calculated using an expansion of the illumination profile in terms of Zernike polynomials. Examples of the correction factor for a typical beam profile from the STARR II source, used with various incident and scattering angle combinations, will be shown. Finally, we will present BRDF measurements taken from 500 nm – 2450 nm on a sintered PTFE (Spectralon)[†] sample. These measurements employed the STARR II light source and a prototype receiver that included both silicon and extended-InGaAs photodetectors on an integrating sphere.

2. STARR II SYSTEM STATUS

Figure 1 shows a schematic of the current status of STARR II, including the light source and the manual arm to allow in-plane BRDF measurements. The light source illuminates the sample with tunable, quasi-monochromatic light, and the scattered light is detected with a broadband, silicon or extended InGaAs photodiode on the receiver. While it would also be possible to illuminate the sample with broadband light from the SC source directly, then detect the scattered light with an array spectrometer, limited dynamic range in spectrometers and limited instrumentation available in the IR beyond 1000 nm make the tunable source approach more suitable to high-accuracy measurements.

2.1 Light source and beam delivery to the sample

The design for the tunable source has been discussed in earlier work,[7] but has undergone some upgrades. The light source is a supercontinuum fiber laser, with broadband output from below 500 nm to greater than 2400 nm. The fiber laser has a bare fiber output, protected by a window, and an off-axis parabolic mirror (OAP) is used to collimate the output. The collimated beam is then coupled into the monochromator, through an order sorting filter wheel (FW), using a translatable lens pair L1 and L2, as described in [7]. The monochromator has a 4-grating turret, and all installed gratings have 600 lines/mm ruling, with differing blaze angles to optimize their performance over different parts of the wavelength range. At the monochromator output, a fused silica holographic diffuser (DIFF) precedes a round aperture (AP) of 500 μm diameter. The diffuser helps to expand the focused spot to fill the aperture. The resulting output from the aperture has approximately 10 nm full-width half maximum (FWHM) bandwidth, and is tunable from 500 nm to 2450 nm.

For BRDF measurements, the quasi-monochromatic light exiting the monochromator aperture must be collected and delivered to a sample 1 m to 2 m away. In the future, the sample plane will be at the center of the robotic-arm based

---

[†] Certain commercial equipment, instruments, software, or materials are identified in this paper to specify the experimental procedure adequately. Such identification is not intended to imply recommendation or endorsement by the National Institute of Standards and Technology, nor is it intended to imply that the materials or equipment identified are necessarily the best available for the purpose.

goniometer. Presently, however, we have set up a manual sample holder and receiver on the optical table adjacent to the source. The aperture is followed by an optical chopper (CH) operating at 75 Hz, to allow lock-in detection of the incident and scattered light. A CaF$_2$ lens, L3, on an automated translation stage, serves to image the circular output aperture to the sample plane, with the help of mirrors (M) for positioning. This produces a well-focused, 1-cm diameter circular illumination area at the sample plane for all operating wavelengths.
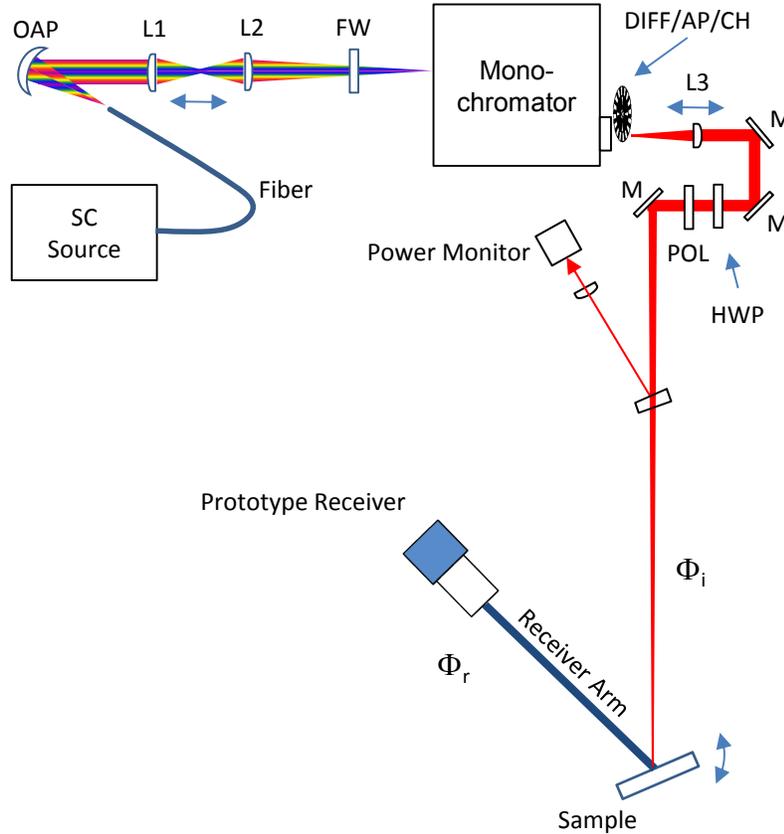

Figure 1**:** Schematic of light source and manual in-plane goniometer (not to scale). OAP = off-axis parabola, L1 – L3 = lenses, FW = filter wheel, DIFF/AP/CH = diffuser, aperture and chopper, M = mirror, HWP = zero-order half-wave plate optimized for 2300 nm, POL = polarizer.

It is also important to consider the polarization of the light reaching the sample. We wish to deliver linearly polarized light, with a rotatable polarization angle, to the sample. For an unpolarized source, the easiest way to accomplish this is by using a rotatable polarizer following the monochromator output. However, we have found that the monochromator output is partially polarized for wavelengths up to about 2000 nm, and more strongly polarized for wavelengths above 2000 nm, due to a combination of polarization dependence of the grating efficiency, and an apparent preferential polarization of the SC source at its longest output wavelengths. Therefore, we set the polarization of the incident flux on the sample, Φ_i, by using the polarizer (POL), but for wavelengths between 1800 nm and 2500 nm, we also use a half-wave plate (HWP) to rotate the plane of polarization of the light source to better match that of the desired polarization angle. The effect on the incident power, particularly when vertically polarized light is desired, is dramatic, and will be discussed in Section 3.1.

3. STARR II LIGHT SOURCE CHARACTERISTICS AND COMPARISON WITH STARR

In this section, we present measured power versus wavelength and polarization, and beam profile at the sample plane, for STARR II, and compare with the values of the existing STARR. STARR uses a lamp- and monochromator-based tunable light source, the details of which can be found in Ref. [1].

3.1 Flux at sample plane

Figure 2 shows the IR tunable source flux Φ_i, as a function of wavelength and for horizontal and vertical polarization. One of the goals for STARR II had been to increase the power that can be delivered to the sample in the IR, and the figure demonstrates the improvement in incident flux provided by the SC-based source. The STARR II source typically delivers hundreds of times the flux in the STARR source. However, the figure also shows one of the challenges of the STARR II source; because the supercontinuum output is not as smoothly varying with wavelength as that which is obtained from a lamp the power level can vary significantly as the source is tuned. Therefore, the optimum gain levels on the receiver can change with wavelength and polarization, and must be kept track of when measuring BRDF.
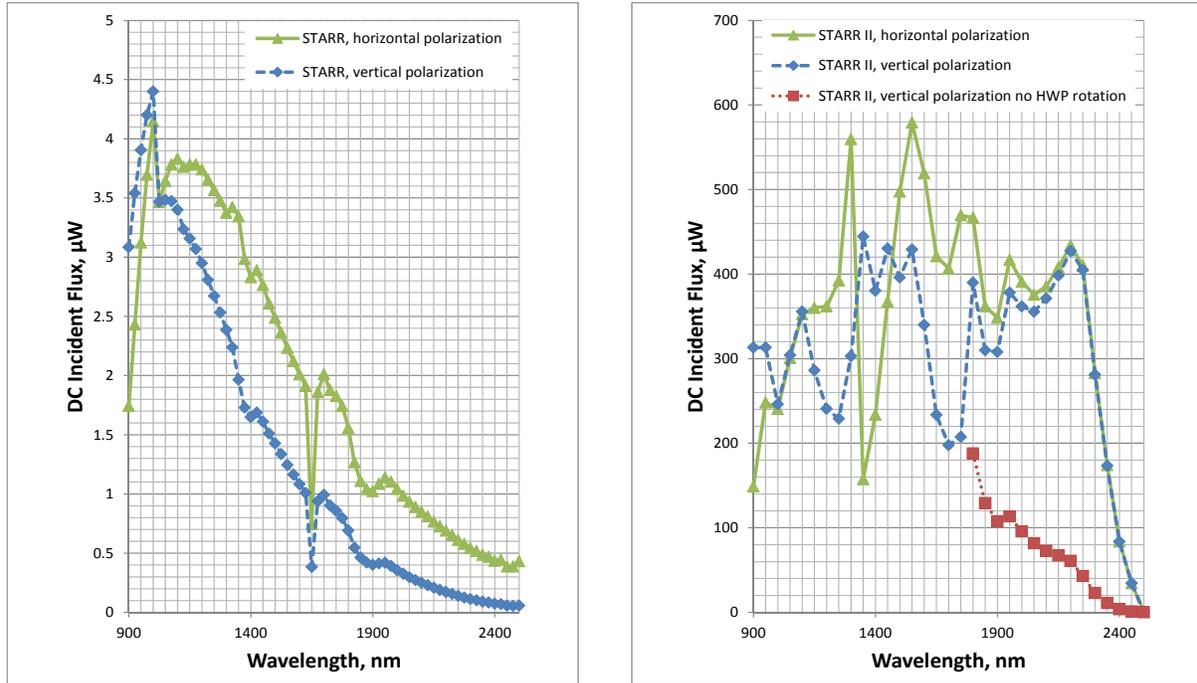

Figure 2: Comparison of tunable incident flux at IR wavelengths from the STARR and STARR II light sources. In both cases, the power was measured using an extended InGaAs photodiode with limited response below 900 nm, so the power at shorter wavelengths is not shown. Uncertainty in the measured flux is estimated to be at the ± 5% level.

Figure 2 also shows that while the power in both STARR and STARR II depend upon the selected polarization, the addition of the half-wave plate in STARR II vastly improves the available power in the vertical polarization state. For comparison, the red dotted/squares trace on the STARR II plot shows the available power in vertical polarization without polarization rotation from the half-wave plate. With the HWP, the available power at the longest wavelengths in STARR II is nearly polarization independent. One limitation for measurements in the SWIR in STARR is the vertically polarized source power. The use of the HWP should eliminate this difficulty in STARR II.

3.2 Spatial beam profiles at the sample plane

Figure 3 shows typical beam profiles, measured at the sample plane, for STARR and STARR II. In STARR, the profile was measured using a 700 μm diameter aperture in front of a silicon photodiode that was translated in 500 μm increments across the sample plane. The STARR II profile was measured using a pyroelectric array camera with 100 μm array spacing. Stability of the measured light level at a fixed position within the beam profile was roughly ± 0.5% for the STARR measurement, and ± 3% for the STARR II measurement. The higher noise in the STARR II measurement is believed to be due to the higher noise of the pyroelectric array camera, which was being used at the lower limit of its sensitivity range, compared to that of the silicon photodiode. In STARR, the beam is fairly circularly symmetric and somewhat unfocused, resulting in the slowly decreasing power seen at the beam edges. Similar beam profiles were seen for other wavelengths measured in STARR, although with slightly poorer central uniformity in the IR. In STARR II, the beam delivery optics produces a well-focused image of the output aperture at the sample plane. The beam was profiled for wavelengths over the operating range of the pyroelectric camera (1060 nm and higher) and a sharp focus was seen at

all wavelengths, as well as at visible wavelengths where the beam focus was inspected by eye. However, as seen in the figure, non-circularly-symmetric beam non-uniformities, or hot spots, occur. This effect was even more pronounced before the addition of the diffuser. Without the diffuser at the monochromator output, the illuminated area appeared more like a horizontal line at the sample. We believe this is due to the laser-like input from the supercontinuum source, which focuses to a small point at the monochromator output that is smeared to a line due to the diffraction of the grating, rather than flooding the round aperture. While the hot spots in the beam are somewhat undesirable, we will show that we can account for them at the same time we correct for the effect of the finite size of the illuminated area. The effects of both the finite size of the illuminated area, and of the beam non-uniformity over that area, are discussed in Section 5.
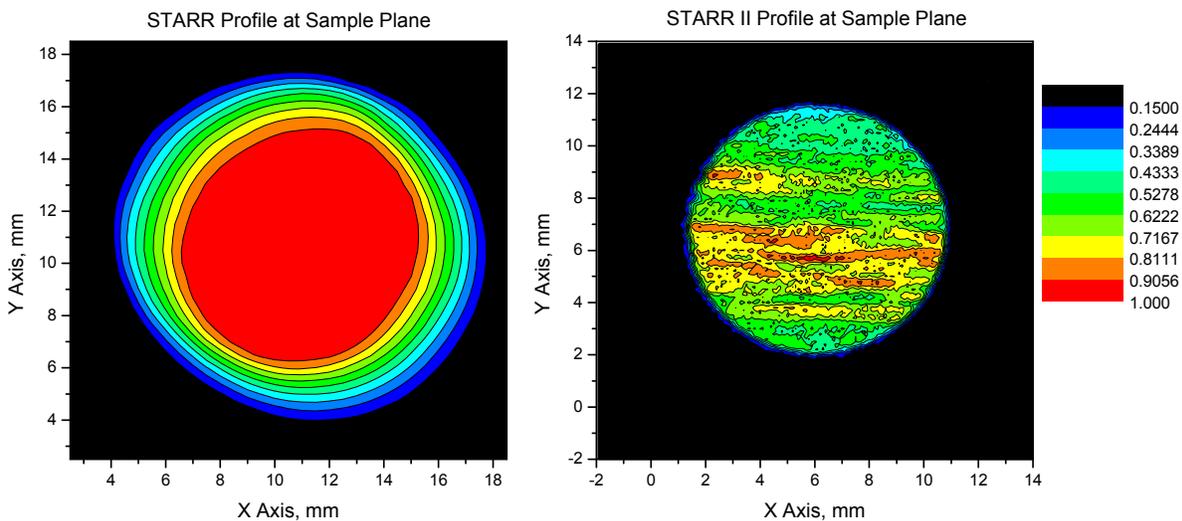

Figure 3: Example incident beam profiles at the sample plane, measured in STARR (left) and STARR II (right). The STARR profile was measured at 550 nm, and the STARR II profile at 1200 nm.

4. BRDF MEASUREMENTS

4.1 Measurement Principle

The manual sample and receiver positioning shown in Figure 1 uses the same measurement principle that will be used in STARR II, and that is currently used in STARR. The near-collimated beam from the light source, with incident flux Φ_i, illuminates the sample at a selectable angle of incidence, θ_i, and a receiver collects the scattered flux Φ_r within a solid angle Ω at polar and azimuthal scattering angles θ_r and ϕ_r. Figure 4 shows the coordinate system with the conventions for θ_i, ϕ_i, θ_r and ϕ_r. The angle ϕ_i is the azimuthal angle of incidence relative to the sample coordinates, which is often taken to be 180°. The receiver has a precision aperture of radius R_a, whose center is located a distance D from the center of the illuminated area on the sample. In the limit of small illuminated area and aperture and large distance, the solid angle of collection is given by

$$\Omega = \frac{\pi R_a^2}{D^2}. \tag{1}$$

The solid angle in fact varies slightly depending upon illumination and viewing geometry, which is discussed in detail in Section 5. In the current set-up shown in Figure 1, the illuminated area is an approximately 10 mm diameter circle at normal incidence (see Figure 3), with nominal receiver aperture and distance $R_a = 12.7$ mm and $D = 588$ mm. Behind the aperture, a lens images the illuminated area of the sample onto the input port of a small integrating sphere. The illuminated area spreads to an ellipse for non-zero θ_i, and the field of view has been made large enough that the illuminated spot on the sample under fills the receiver field stop for incident angles up to 80°. Because we wish to make absolute measurements of BRDF, the receiver must also be able to measure Φ_i. This is accomplished by moving the sample out of the incident beam and swinging the receiver arm around to collect Φ_i. In this position, which we refer to as the total flux position, the incident flux under fills the receiver aperture and the lens focuses the roughly collimated

incident beam into the sphere. Two photodiodes are mounted onto the receiver integrating sphere: a silicon photodiode, which is used for visible to near-IR measurements up to about 1000 nm, and an extended-InGaAs detector, used from 800 nm to 2500 nm. The current from each detector is converted to voltage using a transimpedance amplifier, and the voltages sent to a lock-in amplifier.
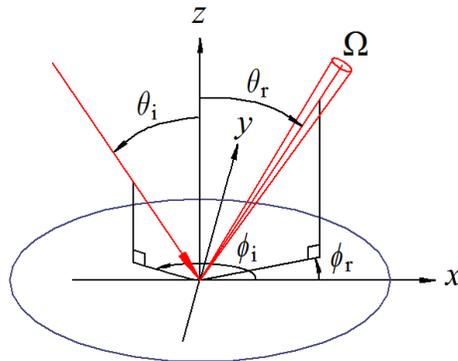

Figure 4: An illustration of the angles typically used to describe BRDF measurement geometries, where the direction of the beam source and receiver are specified with azimuthal and polar angles in the coordinate frame of the sample surface.

The BRDF, f_r, is given by

$$f_{r,\text{meas}}(\theta_i, \phi_i, \theta_r, \phi_r, \lambda, \sigma) = \frac{\Phi_r}{\Phi_i \Omega \cos \theta_r} \qquad (2)$$

where the dependence upon wavelength λ and source polarization σ have been shown along with the angular dependences. Because the BRDF is a multi-parameter function of wavelength, polarization, and geometry, multiple measurement modes (for example, fixed wavelength, scanned viewing angle, or multiple viewing angles with scanned wavelength at each angle) are possible. Here, we discuss the procedure for a fixed geometry, scanned wavelength, polarization averaged measurement, for example, the in-plane 0:45 ($\theta_i = 0°$, $\phi_i = 180°$ incident, $\theta_r = 45°$ $\phi_r = 0°$ viewing) geometry, which can be carried out using the manual set-up shown in Figure 1. We first measure the total flux as a function of wavelength using fixed, horizontal polarization. The sample is then mounted at normal incidence to the beam and the receiver brought to a 45° viewing angle, and the scattered flux is measured versus wavelength. In order to account for any drifts in the source power between total flux and scattered flux measurements, we monitor the source power using the power monitor, which looks at a small portion of the incident beam picked off using a CaF$_2$ window, and normalize the values of Φ_r and Φ_i by the level of the monitor signal. The power monitor also uses an integrating sphere with silicon and extended InGaAs detectors, and is read by a separate lock-in amplifier. Once the measured f_r for horizontal polarization has been obtained, the procedure is repeated for vertically polarized light, and the results at each wavelength are averaged to give the values of f_r that would be obtained for unpolarized light.

4.2 BRDF at arbitrary geometries using robotic arm goniometer

While the existing manual set-up shown in Figure 1 allows only in-plane BRDF geometries, for more general out-of-plane geometries STARR II will employ a robotic arm goniometer to orient the sample, and a rotating arm to position the receiver, as shown in Figure 5. This will allow the BRDF to be measured at nearly any incident and scattering combination in the hemisphere above the sample. In order to operate the goniometer, we need to calculate the required goniometer angles, α, β, γ and δ needed to produce a desired BRDF geometry θ_i, ϕ_i, θ_r and ϕ_r. Knowing the goniometer angles also enables us to calculate the effects of incident beam non-uniformity on the BRDF measurement, since the goniometer angles are needed in order to determine the projection of the beam non-uniformity, which is measured in laboratory frame, onto the angled sample (See Section 5.2). Following Figure 5, the laboratory coordinates are given by (X, Y, Z), and the sample coordinates by (x, y, z) (see also Figure 4). The origin of both coordinate systems is at the center of the goniometer, where the incident beam, which is traveling along $-Z$, intersects the sample. The robotic arm can rotate the sample surface to point in any horizontal or upward direction, and the direction the sample surface is facing in the lab frame can be described by a longitudinal angle α and a latitudinal angle β. The sample can also be

rotated in its plane to any angle γ. The receiver is mounted on an arm which can rotate about the goniometer center to any angle δ in a horizontal plane to measure the scattered flux Φ_r. The sample arm can also move out of the path of the beam and the receiver can be moved to $\delta = 180°$ to measure the incident flux Φ_i. The positive rotation conventions for the angles are as shown in the figure. When $\alpha = \beta = \gamma = \delta = 0$, the normal of the sample face is oriented along the laboratory Z direction, the laboratory and sample coordinates are superimposed, and the receiver is positioned in front of the sample, blocking the incident light.
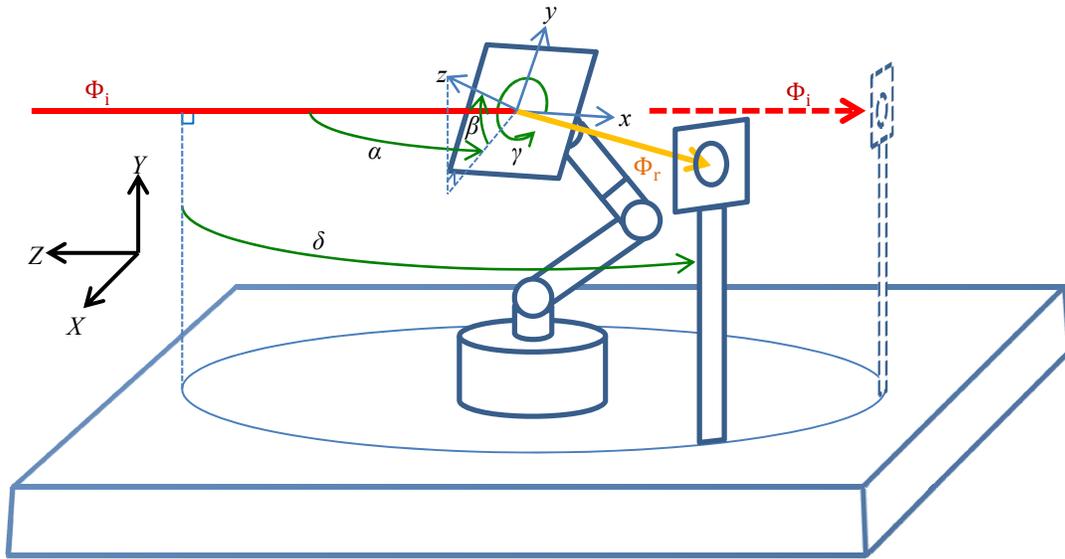

Figure 5: Schematic of the planned robotic arm goniometer for STARR II, showing sample and receiver angles.

The required angle transformations closely follow Germer and Asmail.[8] In brief, the sample and receiver angles required to measure a geometry described by θ_i, ϕ_i, θ_r, and ϕ_r can be calculated as

$$\delta = \text{sgn}(\sin(\phi_r - \phi_i)) \cos^{-1}(\sin\theta_i \sin\theta_r \cos(\phi_i - \phi_r) + \cos\theta_i \cos\theta_r) , \tag{3}$$

$$\alpha = \tan^{-1}\left(\frac{\cos\theta_r - \cos\delta \cos\theta_i}{\sin\delta \cos\theta_i}\right) , \tag{4}$$

$$\beta = \cos^{-1}\left(\frac{\cos\theta_i}{\cos\alpha}\right) , \tag{5}$$

$$\gamma = \begin{cases} \text{atan2}(-\tan\alpha, -\sin\beta) - \varphi_i & \text{if } \theta_i \neq 0 \\ \text{atan2}(\tan(\delta - \alpha), -\sin\beta) - \varphi_r & \text{if } \theta_i = 0 \end{cases} \tag{6}$$

where

$$\text{sgn}(x) = \begin{cases} 1 & \text{if } x \geq 0 \\ -1 & \text{if } x < 0 \end{cases} \tag{7}$$

and

$$\text{atan2}(x, y) = \begin{cases} \tan^{-1}\left(\frac{y}{x}\right) & \text{if } x > 0 \\ \tan^{-1}\left(\frac{y}{x}\right) + \pi & \text{if } x < 0 \\ \frac{\pi}{2} & \text{if } x = 0 \text{ and } y > 0 \\ -\frac{\pi}{2} & \text{if } x = 0 \text{ and } y < 0 \end{cases} \tag{8}$$

These expressions are appropriate for our goniometer configuration, in which it is envisioned that the angle ranges employed will be α (-90°, 90°), β (0°, 90°), γ (0°, 360°), and δ (0°, 360°).

5. BRDF THEORY AND CORRECTION FACTOR FOR SPATIAL BEAM PROFILE

The measurement equation for BRDF given in Eq. (2) is defined as a limit as the receiver aperture subtends a solid angle shrinking to the infinitesimal, and the definition assumes the illumination of the sample surface is concentrated to an infinitesimal point. In a real measurement, however, the incident illumination covers a finite area of the sample, and the collection aperture is also finite, resulting in a variation of the solid angle and the scattering angle depending upon position within the illumination area and collection aperture. The measured BRDF will deviate from Eq. (2) as a result. While these effects are small, Obein et al.[9] have calculated the effect of finite illumination area using a numerical method, for a goniometer with similar geometry to STARR II, and found that in some cases the correction was several tenths of a percent. In this section, we briefly derive an analytic expression for the correction which accounts for both the finite illumination with uniform circular cross-section, and finite circular collection aperture. Because the incident illumination in the current STARR II light source is non-uniform, we then consider the effect of weighted illumination across the circular cross-section, and show that this can be accommodated by expanding the illumination profile in Zernike polynomials. Finally, we present experimental verification of the calculations, obtained by intentionally varying the position of an illumination source around the sample plane and showing that the resulting flux at the receiver followed that expected from theory. We also calculate the correction to Eq. (2) for uniform illumination, and for two representative non-uniform illumination profiles obtained from the STARR II light source. For these calculations, the incident illumination is assumed to be perfectly collimated and the BRDF of the sample is assumed to be uniform.

5.1 Calculation of the correction factor for uniform circular incident illumination

We will work in the sample frame using θ_i, ϕ_i, θ_r, and ϕ_r as standard to describe BRDF measurement geometries, with the origin at the center of the illuminated area on the sample surface as shown in Figure 4. Because we assume the BRDF of the surface to be uniform, we are free to assume $\phi_i = 0$ so that the elongation of the circular incident beam for non-zero θ_i results in an ellipse with major axis along x. The sample surface that can be parameterized by r_s and θ_s as

$$\boldsymbol{r}_s = \left(\frac{r_s}{\cos\theta_i}\cos\theta_s\right)\hat{\boldsymbol{x}} + (r_s\sin\theta_s)\hat{\boldsymbol{y}}, \tag{9}$$

so that circular incident beam illuminates the elliptical area $r_s < R_i$, where R_i is the radius of the beam measured perpendicular to the beam. We will describe measurement geometries using the difference ϕ between the azimuthal angles of incidence and scattering:

$$\phi = \phi_r - \phi_i \tag{10}$$

We wish to describe the direction and position of the receiver aperture relative to the sample frame for any scattering direction. The first step is to rotate the receiver. Since we set the light source to always approach along the negative x-axis, the azimuthal angle ϕ describes how the receiver rotates about the z-axis, and when $\phi_r = 0$ the receiver's polar angle, θ_r, describes how the receiver rotates about the y-axis. Therefore, the rotation of the receiver from its position when $\theta_r = \phi_r = 0$ can be described by the rotation matrix

$$\boldsymbol{R}_r = \begin{bmatrix} \cos\phi & -\sin\phi & 0 \\ \sin\phi & \cos\phi & 0 \\ 0 & 0 & 1 \end{bmatrix} \begin{bmatrix} \cos\theta_r & 0 & \sin\theta_r \\ 0 & 1 & 0 \\ -\sin\theta_r & 0 & \cos\theta_r \end{bmatrix} = \begin{bmatrix} \cos\theta_r\cos\phi & -\sin\phi & \sin\theta_r\cos\phi \\ \cos\theta_r\sin\phi & \cos\phi & \sin\theta_r\sin\phi \\ -\sin\theta_r & 0 & \cos\theta_r \end{bmatrix}. \tag{11}$$

The receiver has a circular aperture at a distance D from the center of the sample surface and faces directly towards the center of the sample. The position of the center of the receiver aperture is then

$$\boldsymbol{r}_{a,\text{center}} = D\boldsymbol{R}_r\hat{\boldsymbol{z}} = D\begin{bmatrix} \sin\theta_r\cos\phi \\ \sin\theta_r\sin\phi \\ \cos\theta_r \end{bmatrix}. \tag{12}$$

The circular receiver aperture of radius R_a can be parameterized by r_a and θ_a as

$$\boldsymbol{r}_{\mathrm{a}} = \boldsymbol{r}_{\mathrm{a,center}} + \boldsymbol{R}_{\mathrm{r}}[(r_{\mathrm{a}}\cos\theta_{\mathrm{a}})\hat{\boldsymbol{x}} + (r_{\mathrm{a}}\sin\theta_{\mathrm{a}})\hat{\boldsymbol{y}}]. \tag{13}$$

Tildes will be used to indicate when a variable is a function of specific values of $\boldsymbol{r}_{\mathrm{s}}$ and $\boldsymbol{r}_{\mathrm{a}}$ where it otherwise might not be clear. Thus, while θ_{r} and ϕ describe the scattering direction the receiver is positioned to measure, the direction of $\boldsymbol{r}_{\mathrm{a,center}}$, $\tilde{\theta}_{\mathrm{r}}$ and $\tilde{\phi}_r$ describe the direction traveled by light from any $\boldsymbol{r}_{\mathrm{s}}$ arriving at $\boldsymbol{r}_{\mathrm{a}}$.

Light from $\boldsymbol{r}_{\mathrm{s}}$ to $\boldsymbol{r}_{\mathrm{a}}$ travels a distance

$$\tilde{r} = |\boldsymbol{r}_{\mathrm{a}} - \boldsymbol{r}_{\mathrm{s}}|. \tag{14}$$

As the aperture is facing the center of the sample surface, $\boldsymbol{r}_{\mathrm{a,center}}$ is normal to the aperture plane, and the light from any $\boldsymbol{r}_{\mathrm{s}}$ arriving at $\boldsymbol{r}_{\mathrm{a}}$ is incident on the aperture at an angle $\tilde{\rho}$ with cosine

$$\cos\tilde{\rho} = \frac{(\boldsymbol{r}_{\mathrm{a}}-\boldsymbol{r}_{\mathrm{s}})\cdot\boldsymbol{r}_{\mathrm{a,center}}}{|\boldsymbol{r}_{\mathrm{a}}-\boldsymbol{r}_{\mathrm{s}}||\boldsymbol{r}_{\mathrm{a,center}}|}. \tag{15}$$

The cosine of the scattering angle for light from any $\boldsymbol{r}_{\mathrm{s}}$ arriving at $\boldsymbol{r}_{\mathrm{a}}$ can be expressed as

$$\cos\tilde{\theta}_{\mathrm{r}} = \frac{(\boldsymbol{r}_{\mathrm{a}}-\boldsymbol{r}_{\mathrm{s}})\cdot\hat{\boldsymbol{z}}}{|\boldsymbol{r}_{\mathrm{a}}-\boldsymbol{r}_{\mathrm{s}}|}. \tag{16}$$

From the integral expression for received flux from BRDF,[10] the total power incident on the receiver aperture from the entire illuminated area can be expressed as a multiple integral.

$$\Phi_{\mathrm{r}} = \frac{1}{\cos\theta_i}\int_0^{2\pi}\int_0^\infty\int_0^{2\pi}\int_0^{R_{\mathrm{a}}} f_{\mathrm{r}}(\theta_i, 0, \tilde{\theta}_{\mathrm{r}}, \tilde{\phi}_{\mathrm{r}})\, E(r_{\mathrm{s}}, \theta_s)\frac{\cos\tilde{\rho}}{\tilde{r}^2}\cos\tilde{\theta}_{\mathrm{r}}\, r_{\mathrm{a}}r_{\mathrm{s}}dr_{\mathrm{a}}\, d\theta_{\mathrm{a}}\, dr_{\mathrm{s}}\, d\theta_s \tag{17}$$

where $E(r_{\mathrm{s}}, \theta_s)$ is the irradiance incident on the sample surface at $\boldsymbol{r}_{\mathrm{s}}$.

If the beam is perfectly uniform, then the irradiance is the total incident power divided by the area of the illuminated ellipse.

$$E(r_{\mathrm{s}}, \theta_s) = \begin{cases} \dfrac{\Phi_i\cos\theta_i}{\pi R_i^2} & \text{if } r_{\mathrm{s}} < R_i \\[2mm] 0 & \text{if } r_{\mathrm{s}} > R_i \end{cases} \tag{18}$$

Then, by expanding the integrand in equation (17) as a Taylor series about the center of the illuminated area and the center of the receiver aperture, integrating, keeping lowest terms, and dividing by equation (2), it can be found that if the sample has a uniform true BRDF f_{r}, then the measured BRDF deviates by a factor of

$$\frac{f_{\mathrm{r,meas}}}{f_{\mathrm{r}}} \approx 1 - \frac{R_{\mathrm{a}}^2}{D^2} + \frac{R_i^2}{D^2}\frac{1}{\cos^2\theta_i}\left[\cos(2\phi)\sin^2\theta_i\sin^2\theta_{\mathrm{r}} - \cos(2\theta_{\mathrm{r}})\frac{3+\cos(2\theta_i)}{4}\right]. \tag{19}$$

We have compared the results of this correction factor with those obtained using a numerical analysis similar to that used by Obein[9] and found that they agree at better than the 0.01% level. As might be expected, the largest corrections are obtained for large values of θ_i because the incident beam is spread over a large area of the sample. Examples of Eq. (19) will be given in Section 5.3.

5.2 Correction factor with non-uniform illumination

If the beam profile is not a uniform circle, its profile can be represented by an expansion in Zernike polynomials[11],

$$E(r_{\mathrm{s}}, \theta_s) = \sum_{m,n} z_n^m\, Z_n^m\left(\frac{r_{\mathrm{s}}}{R_{\mathrm{z}}}, \theta_s\right) \tag{20}$$

where z_n^m are coefficients of the Zernike polynomials $Z_n^m(r, \theta)$, and R_{z} is the radius of a circle large enough to entirely contain the region in which the beam has nonzero irradiance. For a given beam profile, the coefficients can be found as

$$z_n^m = \frac{2n+2}{\epsilon_m\pi R_{\mathrm{z}}^2}\int_0^{2\pi}\int_0^{R_{\mathrm{z}}} E(r_{\mathrm{s}}, \theta_s)\, Z_n^m\left(\frac{r_{\mathrm{s}}}{R_{\mathrm{z}}}, \theta_s\right) r_{\mathrm{s}}dr_{\mathrm{s}}d\theta_s \tag{21}$$

where

$$\epsilon_m = \begin{cases} 2 & \text{if } m = 0 \\ 1 & \text{if } m \neq 0 \end{cases} \tag{22}$$

Again substituting into equation (17), expanding, integrating, keeping lowest terms, and dividing, an expression can be found for the factor by which the instrument will measure a BRDF differing from the true BRDF of the sample.

$$
\begin{aligned}
\frac{f_{r,\text{meas}}}{f_r} \approx{}& 1 - \frac{R_a^2}{D^2} + \left(1 + \frac{1}{3}\frac{z_2^0}{z_0^0}\right)\frac{R_z^2}{D^2}\frac{1}{\cos^2\theta_i}\left[\cos(2\phi)\sin^2\theta_i\sin^2\theta_r - \cos(2\theta_r)\frac{3+\cos(2\theta_i)}{4}\right]\\
&- \frac{z_1^1}{z_0^0}\frac{R_z}{D}\frac{3\sin\theta_r}{4}\left[\cos\psi_i\frac{\cos\phi}{\cos\theta_i} - \sin\psi_i\sin\phi\right]\\
&- \frac{z_1^{-1}}{z_0^0}\frac{R_z}{D}\frac{3\sin\theta_r}{4}\left[\sin\psi_i\frac{\cos\phi}{\cos\theta_i} + \cos\psi_i\sin\phi\right]\\
&+ \frac{z_2^2}{z_0^0}\frac{R_z^2}{D^2}\frac{2}{3\cos^2\theta_i}\left[\cos(2\psi_i)\left(\cos(2\phi)\sin^2\theta_r\frac{3+\cos(2\theta_i)}{4} - \sin^2\theta_i\frac{\cos(2\theta_r)}{4}\right)\right.\\
&\qquad\qquad\qquad\qquad\qquad\left. - \sin(2\psi_i)\sin(2\phi)\cos\theta_i\sin^2\theta_r\right]\\
&+ \frac{z_2^{-2}}{z_0^0}\frac{R_z^2}{D^2}\frac{2}{3\cos^2\theta_i}\left[\sin(2\psi_i)\left(\cos(2\phi)\sin^2\theta_r\frac{3+\cos(2\theta_i)}{4} - \sin^2\theta_i\frac{\cos(2\theta_r)}{4}\right)\right.\\
&\qquad\qquad\qquad\qquad\qquad\left. + \cos(2\psi_i)\sin(2\phi)\cos\theta_i\sin^2\theta_r\right]
\end{aligned}
\tag{23}
$$

where ψ_i, indicating the alignment of the beam profile, is the angle between the $\theta_s = 0$ direction in the beam profile to the projection of the sample surface normal vector into the lab X-Y plane, measured counterclockwise. With the motion of the sample and receiver constrained as they are in STARR II, ψ_i is given by

$$\psi_i = \begin{cases} \text{atan2}(\sin\alpha, \tan\beta) & \text{if } \theta_i > 0 \\ 180° - \phi & \text{if } \theta_i = 0 \text{ and } \delta > 0 \\ -\phi & \text{if } \theta_i = 0 \text{ and } \delta < 0 \end{cases} \tag{24}$$

When performing BRDF measurements, the effects of finite beam size, finite receiver aperture size, and non-uniform beam irradiance can be accounted for by dividing by the factor given in equation (23). It is worth noting that the tilt terms z_1^1 and z_1^{-1} are linear in R_z/D and can produce the most significant corrections in most geometries. However, at large θ_i, other terms that increase with $1/(\cos\theta_i)^2$ become increasingly significant.

5.3 Results and Discussion

In this section, we first present experimental verification of the variation in Φ_r with illumination position in the sample plane calculated in Section 5.1. We then give examples for the correction factor calculated from Eq. (23) using measured beam profiles from STARR II.
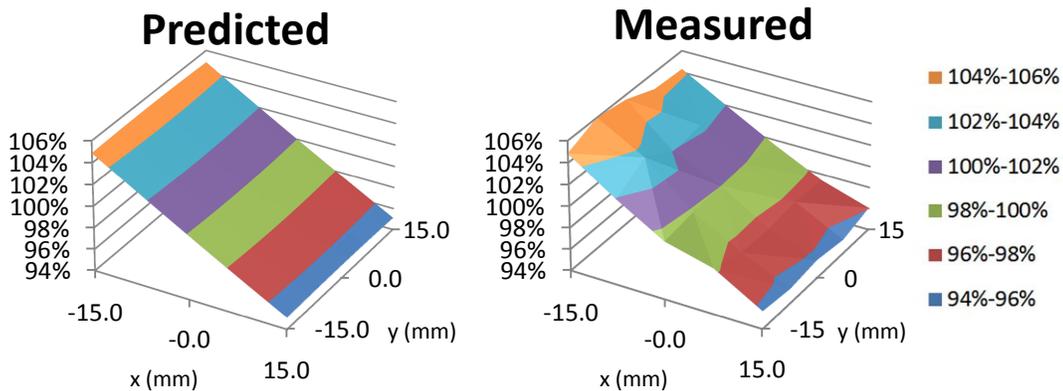

Figure 6: Predicted (left) and measured (right) flux Φ_r seen by the receiver, which was positioned at the $\theta_r = 45°$, $\phi_r = 180°$ position, as a function of the position of a small illumination source translated in the sample x-y plane.

Figure 6 shows the predicted and measured flux Φ_r seen by the receiver as a small illumination source was translated around the x-y sample plane. The illumination source was an integrating sphere, illuminated by an LED, and with a 500 μm diameter aperture installed to define the illumination area. The source was translated in the sample frame x-y plane, with the receiver at the $\theta_r = 45°$, $\phi_r = 180°$ position. The predicted Φ_r was calculated from Eqs. (14)-(17), and normalized to 100% at $x = y = 0$. As expected, higher flux is seen when the illumination source is on the $-x$ side of the sample plane, as the receiver is also on the $-x$ side. We have not fully characterized all sources of uncertainty in this measurement. At a fixed position the stability of the measured Φ_r was typically $\pm 0.5\%$.

In Figure 7, we calculate the correction factor, $f_{r,meas}/f_r$, from Eq. (23) for three cases: a uniform, 10 mm diameter beam, the measured STARR II beam profile at 1200 nm shown in Figure 3, and a third profile measured in STARR II at 1100 nm, that had a larger left-right asymmetry. An incident angle $\theta_i = 80°$ with in-plane geometry was chosen. We used $\theta_i = 80°$ because this is the largest incident angle accommodated by the STARR II receiver field of view, and results in the largest major axis of the elliptical beam. In-plane geometry was chosen because the receiver is constrained to be in the lab X-Z plane, (see Figure 5), and because of this, it is in-plane geometries that cause the receiver to see the largest spread in the beam and generally largest correction factors. For these calculations $R_a = 14.05$ mm and $D = 650$ mm, which are appropriate to the planned robot goniometer.
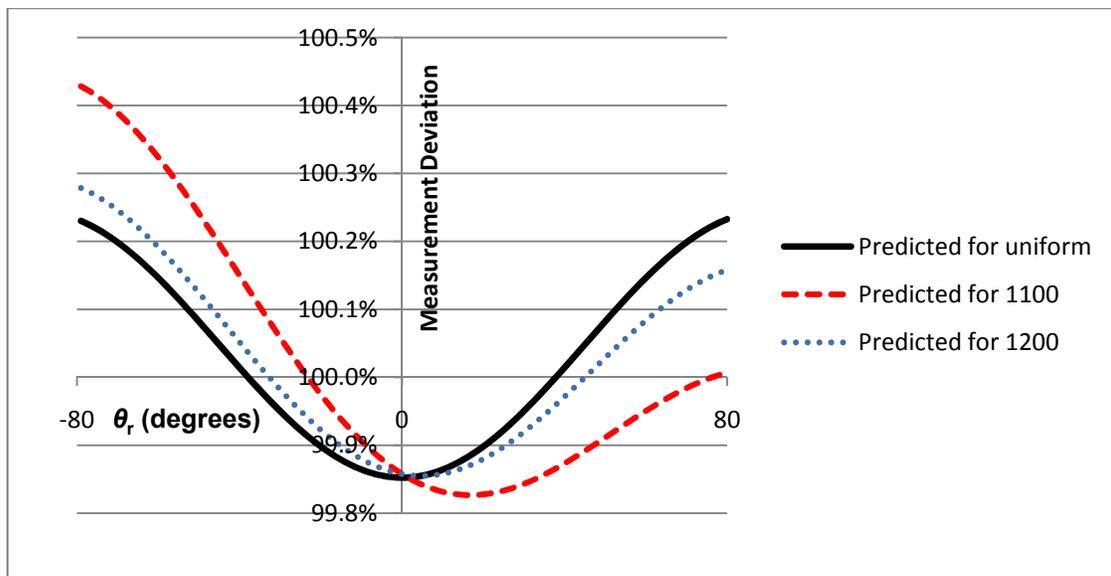

Figure 7: The correction factor, $f_{r,meas}/f_r$, from Eq. (23) for three cases: a uniform, 10 mm diameter beam (solid black), the measured STARR II beam profile at 1200 nm shown in Figure 3 (dotted blue), and a third profile measured in STARR II at 1100 nm, that had a larger left-right asymmetry than at 1200 nm (dashed red). An incident angle of $\theta_i = 80°$ was used. Negative values of θ_r correspond to those where $\phi = 0°$, positive θ_r have $\phi = 180°$.

The correction factor for both uniform and non-uniform illumination can be significant. If the beam profile is non-uniform, particularly with right-left asymmetry, the corrections increase; for example, both the 1200 nm and 1100 nm beam profiles have more light in the $-X$ side of the profile, and in both cases, when the receiver is closer to the $-X$ side (shown as negative θ_r in the Figure), the correction factor increases. This tilt effect is also very sensitive to the centering of the beam in the goniometer; one can easily imagine that if the beam profile is moved slightly along the sample x, a different correction factor will be obtained. We are considering how best to control or account for this in STARR II. The figure and other calculations using Eq. (23) indicate that when accuracy at the 1% level is desired, the finite beam profile size and its non-uniformity are not a large issue. However, for accuracy better than 0.1% they can be significant, particularly for measurements with large θ_i. We also note that the changes in illumination profile with wavelength seen in the current STARR II light source may need to be improved or monitored. We are considering other illumination schemes, such as installing optics for Kohler illumination[12] at the monochromator output to deliver a more uniform illumination area. Finally, while for the calculations shown in Figure 7 the radius for the Zernike polynomials R_z was taken to be the edge of the illumination profile R_i, we have found the results of Eq. (23) to be fairly insensitive to expanding R_z beyond the beam edge.

6. INITIAL BRDF MEASUREMENTS IN STARR II

To demonstrate the use of the wavelength tuning capabilities of the STARR II source for BRDF measurements, and as a platform for investigating the signal to noise and systematic errors of the source and receiver, we have begun making exploratory measurements of BRDF on a 1 cm thick sample of white Spectralon. The sample was mounted manually in an in-plane configuration as shown in Figure 1, with the receiver mounted on a rail that functioned as the receiver arm. BRDF measurements were performed at 0:45 geometry for wavelengths from 500 nm to 2450 nm. The silicon detector was used for wavelengths from 500 nm to 1000 nm, while measurements were made using the extended InGaAs detector from 750 nm to 2450 nm. Data were measured for s- (vertical) and p- (horizontal) polarized incident light, and the results averaged to obtain the BRDF for unpolarized incident light.
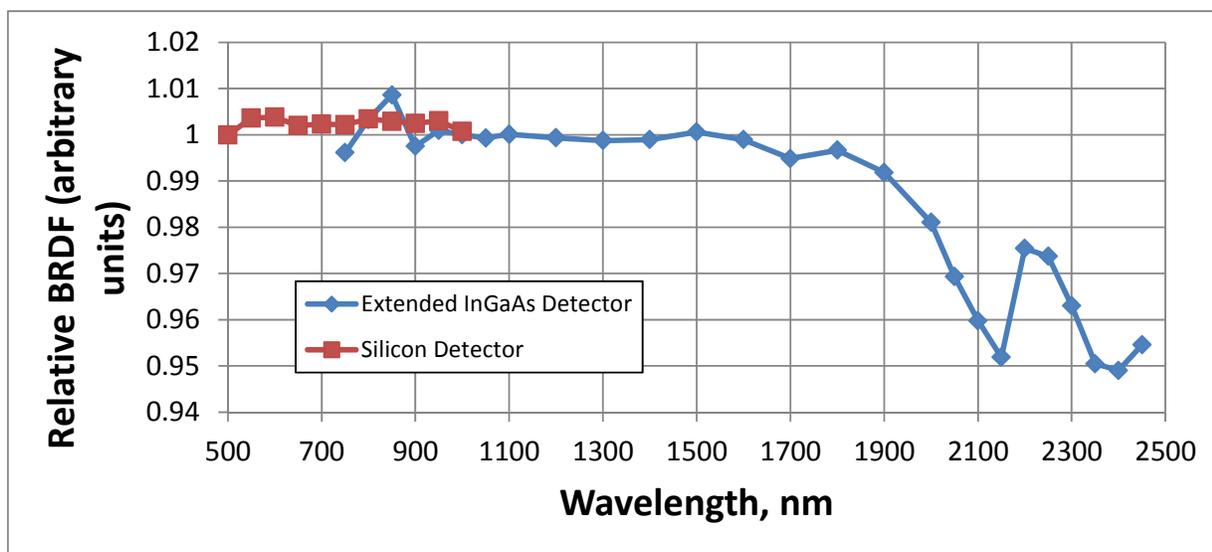

Figure 8: BRDF relative to the BRDF value obtained using the extended-InGaAs detector at 1000 nm, for a 1 cm thick sample of Spectralon. BRDF values are for unpolarized incident light and 0:45 reflectance geometry.

Figure 8 shows typical results. Because the geometric factors in Eq. (2) were known only approximately, we present the BRDF normalized to its value at 1000 nm as measured using the extended InGaAs detector. The shape of the BRDF versus wavelength is similar to that given for a Spectralon sample in Ref. [2], and shows the well-known dip in reflectance around 2150 nm. While we have just begun the error analysis for STARR II, the uncertainty component due to repeatability, as measured by the standard deviation of the mean for 10 consecutive measurements of BRDF at fixed geometry, wavelength, and polarization, was typically 0.1% for both the silicon detector between 600 nm and 1000 nm, and for the extended InGaAs detector between 950 nm and 2350 nm. The repeatability is dominated by the noise in the scattered flux measurement. For the extended InGaAs detector, the noise in the scattered flux measurement was higher for wavelengths below 950 nm and above 2350 nm, and for the silicon detector, higher noise in the scattered flux was seen for wavelengths below 600 nm. We are in the process of identifying and attempting to reduce sources of noise.
For example, for the extended InGaAs detector, both the source flux (Figure 2) and the detector responsivity[13] decrease rapidly with wavelength at the longest wavelengths, above 2350 nm. The scattered flux data for wavelengths with lower source flux and/or lower detector responsivity were generally observed to be noisier.

We are also in the process of looking for systematic errors and evaluating the accuracy of our measurements. In addition to uncertainty in the geometric factors of the set-up, another factor influencing the accuracy of the results is linearity of the detectors over the wide dynamic range seen between the total flux and scattered flux positions. From Eq. (2), it can be calculated that for an example BRDF of 0.3 for a white sample and our nominal geometric factors, the signal at the scattered flux position is more than 3,000 times lower than that at the total flux position. While we have attempted to minimize any problems with gain linearity of the transimpedance amplifiers for the current measurements by using the same gain setting at the total flux and scattered flux positions, we are assuming linearity of the lock-in amplifiers. In the near future, we plan to fully characterize the gain linearity of our amplifiers and lock-ins. This will

also allow us to use higher transimpedance amplifier gains for the scattered flux measurement, which may improve the noise in those measurements.

7. SUMMARY AND FUTURE WORK

We have reported on the status of the SC-based, tunable light source for STARR II, and shown that it delivers a circular, well-defined incident beam to a sample location for measurement of BRDF over the 500 nm to 2450 nm range. Considerations for the accurate measurement of BRDF with this source and a robotic arm-based goniometer have been presented. We have derived an expression that enables us to account for BRDF corrections brought about by the spatial extent of the illuminated area and the receiver aperture, and shown that these corrections can be significant when accuracy better than 1% is required. Finally, we have begun spectral BRDF measurements with this source, a manual goniometer, and a prototype receiver. Future work is expected to include installation and qualification of the goniometer, optimization of the receiver, extension to UV wavelengths using a lamp- or laser-based solution, and detailed characterization of systematic and random sources of error. Comparisons with STARR, as well as other goniometric scatter instruments at NIST[8,9] are also planned.

8. REFERENCES

1. Proctor, J.E. and Barnes, P.Y., "NIST high accuracy reference reflectometer-spectrophotometer," J. Res. Natl. Inst. Stand. Technol. 101, 619-627 (1996). See also http://physics.nist.gov/Divisions/Div844/facilities/brdf/starr.html.
2. Yoon, H.W., Allen, D.W., Eppeldauer, G.P., and Tsai, B.K., "The extension of the NIST BRDF scale from 1100 nm to 2500 nm", Proc. SPIE 7452, 745204 (2009).
3. Tsai, B.K, Allen, D.W., Cooksey, C., Yoon, H.W., Fulton, L., Biggar, S., and Markham, B., "Calibration of LANDSAT/OLI Panels Using the NIST BRDF Scale from 1100 nm to 2400 nm", CALCON Technical Conference, Logan, Utah, 2010.
4. A survey of remote sensing satellites can be found at http://www.crisp.nus.edu.sg/~research/tutorial/optical.htm
5. Huenerhoff, D., Grusemann, U., and Hoepe, A., "New robot-based gonioreflectometer for measuring spectral diffuse reflection", Metrologia 43, S11-S16 (2006).
6. Baribeau, R., Neil, W.S., and Côté, E., "Development of a robot-based gonioreflectometer for spectral BRDF measurement", Journal of Modern Optics, 56: 13, 1497-1503 (2009).
7. Zarobila, C.J. and Patrick, H.J., "Supercontinuum fiber laser source for reflectance calibrations in remote sensing," Proc. SPIE 7807, 78070B-1-17 (2010).
8. Germer, T.A. and Asmail, C.C., "Goniometric optical scatter instrument for out-of-plane ellipsometry measurements", Review of Scientific Instruments 70, 3688-3695, (1999).
9. Obein, G., Bousquet, R., and Nadal, M.E., "New NIST Reference Goniospectrometer", Proc. SPIE 5880, 58800T1-10 (2005).
10. Nicodemus, F.E., Richmond, J.C., Hsia, J.J., Ginsberg, I.W. and Limperis., T., "Geometrical Considerations and Nomenclature for Reflectance", NBS Monograph 160, National Bureau of Standards, pg. 11, (1977).
11. For an overview of Zernike polynomials, see http://www.optics.arizona.edu/jcwyant/zernikes/ZernikePolynomialsForTheWeb.pdf
12. Bass, M., ed., [Handbook of Optics, Vol. 1], McGraw-Hill, Inc., page 32.11, (1995).
13. Teledyne-Judson catalog, "Indium Gallium Arsenide Detectors", available at http://www.judsontechnologies.com/files/pdf/InGaAs_shortform_DEC2004_rev2.pdf